Journal of Advanced Ceramics
2019, **8**(3): 352–366
https://doi.org/10.1007/s40145-019-0317-5

ISSN 2226-4108
CN 10-1154/TQ

Research Article

Effect of calcination temperature on structural and optical properties of MAl_2O_4 (M = Ni, Cu, Zn) aluminate spinel nanoparticles

Thanit TANGCHAROEN[a,*], Jiraroj T-THIENPRASERT[b], Chanapa KONGMARK[c]

[a]*Department of Basic Science and Physical Education, Faculty of Science at Sriracha, Kasetsart University, Sriracha Campus, Chonburi 20230, Thailand*
[b]*Department of Physics, Faculty of Science, Kasetsart University, Bangkok 10900, Thailand*
[c]*Department of Materials Science, Faculty of Science, Kasetsart University, Bangkok 10900, Thailand*

Received: September 28, 2018; Revised: January 11, 2019; Accepted: January 18, 2019
© The Author(s) 2019.

Abstract: $NiAl_2O_4$, $CuAl_2O_4$, and $ZnAl_2O_4$ aluminate spinel nanoparticles were synthesized by sol-gel auto combustion method using diethanolamine (DEA) as a fuel. The effects of calcination temperature on structure, crystallinity, morphology, and optical properties of MAl_2O_4 (M = Ni, Cu, Zn) have been investigated by X-ray diffraction (XRD), Fourier transform infrared spectroscopy (FT-IR), scanning electron microscopy (SEM), UV–visible diffuse reflectance spectroscopy (UV-DRS), and photoluminescence (PL) spectroscopy. The XRD and FT-IR results confirm the formation of single-phase spinel structure of $NiAl_2O_4$, $CuAl_2O_4$, and $ZnAl_2O_4$ at 1200, 1000, and 600 ℃, respectively. The direct band gap of these aluminate spinels, calculated from UV-DRS spectra using the Kubelka–Munk function, is found to increase with calcination temperature. The PL spectra demonstrate that $NiAl_2O_4$ gives the highest blue emission intensity, while $CuAl_2O_4$ and $ZnAl_2O_4$ exhibit a very strong violet emission. During fluorescence process, the $ZnAl_2O_4$ emits visible light in only violet and blue regions, while $NiAl_2O_4$ and $CuAl_2O_4$ emissions extend to the green region. It seems therefore that the transition metal type and intrinsic defects in these aluminate powders are responsible for these phenomena.

Keywords: $NiAl_2O_4$; $CuAl_2O_4$; $ZnAl_2O_4$; sol-gel auto combustion; diethanolamine (DEA); photoluminescence (PL)

1 Introduction

Metal aluminate spinels with the formula MAl_2O_4, where M represents a divalent metal ion, have attracted great attention for various applications owning to their high chemical and thermal stabilities, high mechanical resistance, high quantum yields with hydrophobic qualities, large surface area, and low surface acidity [1–3]. They have been widely used as photocatalysts, refractories, pigments, sensor, and magnetic, optical, and electrode materials including lubricant additive [4–7]. It has long been known that the synthesis method can affect the purity, crystallinity, surface area, particle size, and morphology of nanocrystalline MAl_2O_4, which exert a significant influence on their optical and catalytic properties [8–10]. MAl_2O_4 can be prepared by various techniques including solid-state reactions, co-precipitation synthesis, sol-gel method, solvothermal method, hydrothermal method, microwave-assisted hydrothermal

* Corresponding author.
E-mail: sfscitnt@ku.ac.th

method, and polymeric precursor synthesis [8–10]. Each of these techniques requires its own specialized equipment, imposing significant cost, while further drawbacks include the low surface area of product and lack of homogeneity [3,11]. The sol-gel auto combustion method has been demonstrated to produce homogeneous high-purity nanoparticles with rapid heating and short reaction time [12–14]. This synthesis method combines the chemical sol-gel and combustion process, representing a quick, accessible technique with low energy costs and ideal for the synthesis of materials based on metal oxides. Various organic compounds can be employed as the fuel, but these have been conventionally limited to urea, citric acid, tartaric acid, and glycine [15,16]. In our previous studies, we have recently demonstrated the potential use of diethanolamine (DEA) as a novel fuel for sol-gel auto combustion synthesis of nanocrystalline $NiAl_2O_4$, $CuAl_2O_4$, and $ZnAl_2O_4$ aluminate spinels [17]. The obtained nano-size aluminate particles exhibited a single phase cubic spinel structure with excellent photocatalytic degradation of phenol rhodamine B (RhB), heteropolyaromatic methylene blue (MB), azoic methyl orange (MO), and methyl red (MR) under ultraviolet irradiation. $NiAl_2O_4$ and $CuAl_2O_4$ are found to exhibit higher photocatalytic activities than $ZnAl_2O_4$ due to the difference in band gap energy. The E_g value of $ZnAl_2O_4$ (5.5 eV) is much larger than those of $NiAl_2O_4$ and $CuAl_2O_4$ (3.45 and 3.00 eV, respectively), which would limit the UV absorption region to very short wavelengths. It is obvious that the optical properties should play an important role in the photocatalytic performance of these materials. However, a comparative study of the influence of calcination temperature on the structure and optical properties of these materials has not yet been clarified. Aguilar *et al.* [18] studied the phase evolution of Cu–Al–O powders which were prepared by the Pechini method and calcined at different temperatures. $CuAl_2O_4$ and CuO were observed as intermediate phases at 900 and 1000 ℃ before transforming to $CuAlO_2$ final phase at 1100 ℃. Nazemi *et al.* [19] investigated the effect of calcination temperature on $NiAl_2O_4$ powders synthesized by mechano-chemical process. The single phase $NiAl_2O_4$ spinel powders were obtained at 1400 (unmilled powders) and 1100˚C (15 h milled powders) ; however, their optical properties have not been examined. Cornu *et al.* [20] studied the luminescence properties of $ZnAl_2O_4$ particles which were prepared using the Pechini or co-precipitation synthetic route and treated at different temperatures between 600 and 1350 ℃. It was found that the transformation of amorphous precursor to $ZnAl_2O_4$ spinel phase occurred after heat treatment at 600 ℃ and various luminescence emissions linked to the presence of defects in the matrix structure. To the best of our knowledge, there have been no studies comparing the effect of calcination temperature on the structural and optical properties of $NiAl_2O_4$, $CuAl_2O_4$, and $ZnAl_2O_4$ aluminate spinels which were prepared by the same synthesis method.

In the present study, the $NiAl_2O_4$, $CuAl_2O_4$, and $ZnAl_2O_4$ aluminate spinels were synthesized by the sol-gel auto combustion method and calcined at different temperatures (600, 800, 1000, and 1200 ℃). The effects of divalent metal ions and calcination temperatures on the structure, surface morphology, and optical properties of aluminate spinel (MAl_2O_4 (M = Ni, Cu, Zn)) have been investigated by X-ray diffraction (XRD), Fourier transform infrared spectroscopy (FT-IR), scanning electron microscopy (SEM), transmission electron microscopy (TEM), UV–visible diffuse reflectance spectroscopy (UV-DRS), and photoluminescence (PL) spectroscopy techniques. The optical properties and photoluminescence mechanisms of these metal aluminates are elucidated.

2 Experimental

2.1 Materials

The raw materials used for the preparation of $NiAl_2O_4$, $CuAl_2O_4$, and $ZnAl_2O_4$ aluminate spinels include $Ni(NO_3)_2{\cdot}6H_2O$ (nickel nitrate hexahydrate), $Cu(NO_3)_2{\cdot}3H_2O$ (copper nitrate trihydrate), $Zn(NO_3)_2{\cdot}6H_2O$ (zinc nitrate hexahydrate), $Al(NO_3)_3{\cdot}9H_2O$ (aluminum nitrate nonahydrate), and $C_4H_{11}NO_2$ (diethanolamine, DEA). All chemical reagents are of analytical grade and used as received without further purification.

2.2 Preparation of $NiAl_2O_4$, $CuAl_2O_4$, and $ZnAl_2O_4$

The $NiAl_2O_4$, $CuAl_2O_4$, and $ZnAl_2O_4$ nanoparticles were synthesized by the sol-gel auto combustion method [17]. First, stoichiometric amounts of metal nitrate and aluminum nitrate were dissolved in absolute ethanol to obtain a 0.2 mol/L solution. Then, an appropriate amount of DEA was added as fuel into the solution. The mixture was heated to 200 ℃ while stirring constantly. The mixed solution transformed into a condensed gel,

which self-ignited to produce a pearl white foamy product for $ZnAl_2O_4$ and dark brown powders for $NiAl_2O_4$ and $CuAl_2O_4$. Finally, the as-synthesized powders were calcined in air at 600, 800, 1000, and 1200 ℃ for 4 h.

2. 3 Characterizations

The phase composition of the obtained powders was analyzed by XRD using a PANalytical X'Pert PRO MPD diffractometer and with Cu Kα radiation (λ = 1.5406 Å). The XRD patterns were collected from 20° to 80° with scanning steps of 0.04° and time step of 0.1 s. The FT-IR spectra of samples were recorded on a thermo scientific infrared spectrometer (Nicolet 6700) with KBr pellets in transmission mode, in the frequency range of 400–4000 cm^{-1}. Particle size and morphology were investigated by scanning electron microscopy (SEM, LEO 1450VP) and transmission electron microscopy (TEM, TECNAI G2). The samples were coated with gold for better visibility of the surface morphology for SEM measurement. In the process of preparing the TEM specimen, a small amount of the powder was dispersed in ethanol in an ultrasonic bath, and a few drops of the resulting suspension were placed on to a carbon-coated copper grid. UV–visible diffuse reflectance spectra were recorded using an Agilent Cary 5000 UV–Vis NIR spectrometer with an attached diffuse reflectance accessory in the wavelength range of 200–1000 nm to determine the energy band gap of the samples. Room temperature PL properties were studied by Perkin Elmer LS55 fluorescence spectrophotometer.

3 Results and discussion

3. 1 XRD analysis

XRD was used to identify the crystal structure and phase evolution of $NiAl_2O_4$, $CuAl_2O_4$, and $ZnAl_2O_4$ powders after calcination at various temperatures (600, 800, 1000, and 1200 ℃). Figure 1(a) shows the development of $NiAl_2O_4$ spinel structure. The as-synthesized powders exhibit diffraction peaks corresponding to NiO and Al_2O_3 phases, in agreement with JCPDS Nos. 45-0937 and 46-1212, respectively [21]. The characteristic peaks of $NiAl_2O_4$ first appear after calcination at 800 ℃. As the calcination temperature rises, the intensity of $NiAl_2O_4$ peaks gradually increases at the expense of NiO and Al_2O_3. The powders calcined at 1000 ℃

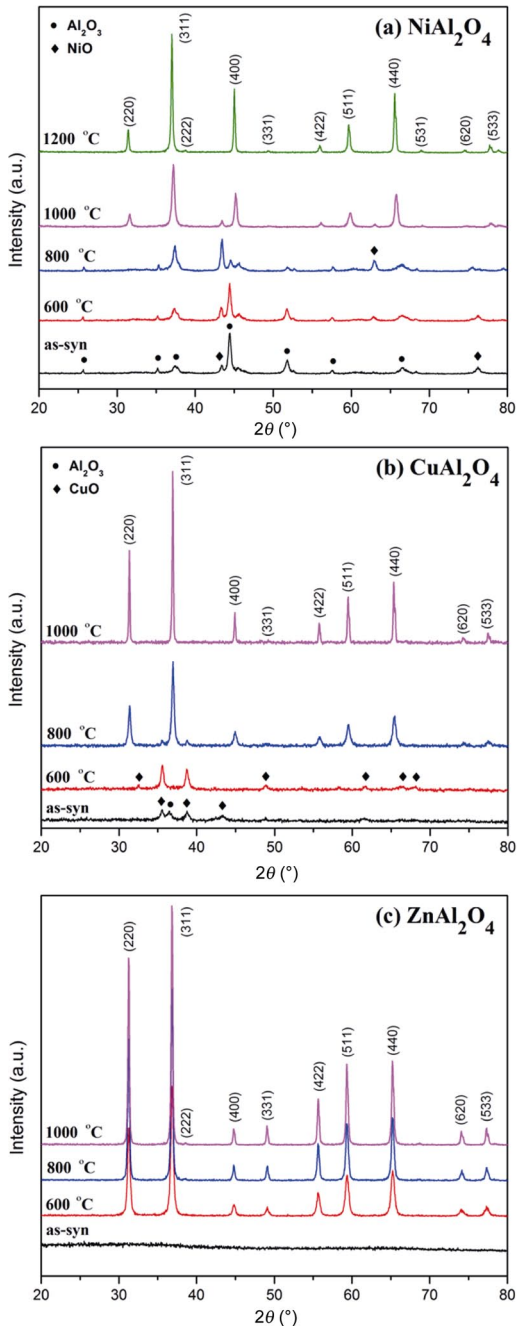

Fig. 1 XRD patterns of (a) $NiAl_2O_4$, (b) $CuAl_2O_4$, and (c) $ZnAl_2O_4$ powders calcined at different temperatures.

consist of the major phase $NiAl_2O_4$ with a trace amount of NiO. At the calcination temperature of 1200 ℃, NiO completely disappears and a single phase $NiAl_2O_4$ is obtained. The observed diffraction peaks are assigned to a cubic spinel structure of nickel aluminate (JCPDS No. 10-0339) [22–24]. The strong sharp diffraction peaks indicate that $NiAl_2O_4$ calcined at 1200 ℃ has a long-range ordered structure. These results correlate well with the previous study by Nazemi *et al.* [19] who

found that a mixture of NiO and Al_2O_3 powders transformed to the single phase $NiAl_2O_4$ spinel powders after calcination above 1000 ℃, at 1100 ℃ for 15 h milled powders, and at 1400 ℃ for unmilled powders. For the $CuAl_2O_4$ samples (Fig. 1(b)), a monoclinic structure of CuO (JCPDS No. 45-0937) and a small impurity phase of Al_2O_3 [25,26] are found in the as-synthesized powders. When the powders are calcined at 600 ℃, the XRD peak intensity of CuO increases while the characteristic peaks of Al_2O_3 disappear. At 800 ℃, the formation of $CuAl_2O_4$ phase occurs but the CuO trace still remains. Similar phase evolution has been observed for Cu–Al–O powders which were prepared by the Pechini method and calcined at different temperatures [18]. Aguilar *et al.* [18] identified $CuAl_2O_4$ and CuO as intermediate phases at 900 and 1000 ℃ before transforming to $CuAlO_2$ final phase at 1100 ℃. Mindru *et al.* [27] also found the presence of CuO as an impurity phase in the $CuAl_2O_4$ samples calcined at 900 ℃. In the present study, a single phase $CuAl_2O_4$ aluminate spinel (JCPDS No. 33-0448) is obtained after calcination at 1000 ℃ [23,28]. The formation process of $ZnAl_2O_4$ spinel structure is different from those of $NiAl_2O_4$ and $CuAl_2O_4$. The as-synthesized $ZnAl_2O_4$ powders are amorphous which later transform into a highly crystalline $ZnAl_2O_4$ aluminate spinel structure (JCPDS No. 05-0669) [29–31] after calcination at 600 ℃. This is in agreement with previous studies by Cornu *et al.* [20]. They also found that the amorphous precursor, obtained from the Pechini or co-precipitation synthetic route, transformed into $ZnAl_2O_4$ spinel phase after heat treatment at 600 ℃. Further increasing calcination temperature leads to diffraction with sharp, narrow, and high-intensity peaks, indicating an increase in crystallinity and particle size of $ZnAl_2O_4$.

In addition, the average crystallite size (D) of single-phase spinel samples can be estimated from the full width at half maximum of the strongest diffraction peak (311) by applying Debye–Scherrer equation:

$$D = \frac{0.9\lambda}{\beta \cos\theta} \tag{1}$$

where D is the average crystallite size, λ is the wavelength of the X-ray source (Cu Kα, 1.54 Å), β is the integral breadth of the (311) diffraction peak, and θ is the Bragg's diffraction angle. The width of the Bragg peak is the combination of both sample and instrument broadening effects. The latter can be determined using a standard material such as silicon. The corrected peak width β, corresponding to the diffraction peak of the samples can be estimated using the following relationship:

$$\beta = (\beta^2_{\text{measured}} - \beta^2_{\text{instrumental}})^{\frac{1}{2}} \tag{2}$$

Consequently, interplanar spacing (d_{hkl}) and lattice parameter (a) of these samples are determined using Eqs. (3) and (4), respectively.

$$d_{hkl} = \frac{\lambda}{2\sin\theta} \tag{3}$$

$$a = d_{hkl}(h^2 + k^2 + l^2)^{\frac{1}{2}} \tag{4}$$

The calculated results are presented in Table 1. The lattice parameter of aluminate spinels is in the order of $NiAl_2O_4 < CuAl_2O_4 < ZnAl_2O_4$, which should be related to the difference in ionic radius of transition metals. The average crystallite sizes of $NiAl_2O_4$, $CuAl_2O_4$, and $ZnAl_2O_4$ (calcined at 1000 ℃) are 42, 62, and 42 nm, respectively. The results of $ZnAl_2O_4$ powders correlate well with those reported by Ianoş *et al*. [12] and Visinescu *et al*. [14] who applied a combustion synthesis method using starch and urea as fuel. Moreover, the average crystallite size and lattice parameter of $ZnAl_2O_4$ are found to increase with the calcination temperature. Similar results have been reported by Cornu *et al.* [20] whose as-synthesized $ZnAl_2O_4$ spinel powders were calcined at different temperatures. They found that the crystallite size significantly increased from 4.7 to 57.8 nm when the calcination temperature was raised from 600 to 1000 ℃. Parra and Haque [32] also mentioned that when the temperature increases, the nucleation rate of the particles increases more rapidly. This can be explained by the increase in supersaturation of the reaction products, which accelerates the crystal core forming reaction within a short time. The crystallite size thus increases as a result of this process. For $NiAl_2O_4$ and $CuAl_2O_4$, they show similar lattice parameters and larger crystallite sizes compared to those obtained by the combustion method using glycine as fuel and calcined at lower temperatures (600 and 900 ℃) [26,33]. This difference is likely due to the variation in calcination temperatures and different types of fuel. A similar observation has been reported for $CoAl_2O_4$ ceramic pigment prepared by means of solution combustion synthesis method using different fuels [34]. The crystallite size of aluminate sample synthesized with urea (9 nm) is obviously smaller than that of glycine (19 nm). Gilabert

Table 1 Average crystallite size (*D*), interplanar distance (*d*), lattice parameter (*a*), and band gap value (E_g) of single-phase $NiAl_2O_4$, $CuAl_2O_4$, and $ZnAl_2O_4$ powders

Sample	*D* (nm)	$d_{(311)}$ (Å)	*a* (Å)	E_g (eV)
$NiAl_2O_4$ (1200 ℃)	42	2.428	8.053	3.45
$CuAl_2O_4$ (1000 ℃)	62	2.435	8.076	3.00
$ZnAl_2O_4$ (1000 ℃)	42	2.440	8.092	5.50
$ZnAl_2O_4$ (800 ℃)	35	2.439	8.089	5.42
$ZnAl_2O_4$ (600 ℃)	30	2.438	8.086	5.35

et al. [34] stated that the main difference between fuels lies in the molar ratio of emitted gases/spinel formed. The higher the amount of gaseous products released during combustion, the higher the porous voluminous masses are obtained, but the lower the maximum temperature they achieve in the process because they lose more heat. In the case of urea and glycine, the ratio is approximately 31 and 26 mol gas/spinel, respectively.

3. 2 FT-IR spectroscopy analysis

The typical transmittance FT-IR spectra of as-synthesized and calcined $NiAl_2O_4$, $CuAl_2O_4$, and $ZnAl_2O_4$ powders are shown in Fig. 2 as a series of transmission peaks in the range of 400–4000 cm^{-1}. FT-IR analysis was performed to investigate the formation of metal aluminate spinel structure and the surface functional group. All the samples contain common absorption bands around 3462, 2922, 2850, 2337, 1633, 1385, 1200, and 1118 cm^{-1}. Broad bands near 3462 and 1633 cm^{-1} are attributed to –OH stretching vibrational modes and bending vibrational mode of absorbed water molecules, respectively [35]. Several IR studies of metal aluminate spinels noticed the water absorption peaks and stated that the high surface area of these materials could result in rapid adsorption of water from the atmosphere during pellet compression and IR measurements [35,36]. Small peaks at about 2922 and 2850 cm^{-1} belong to C–H stretching vibration [1]. The absorption band at 2337 cm^{-1} is possibly related to the presence of CO_2 on the powder surface, while a small peak at 1385 cm^{-1} can be attributed to the residual nitrogen groups resulting from the combustion reaction [36]. The peaks in the 1200 cm^{-1} region can be interpreted as vibrations of the C–C bond, and bands at around 1118 cm^{-1} can be attributed primarily to oxygen groups with a single C–O bond [37,38]. Shanaj and John [39] reported that these organic impurities could be reduced by increasing

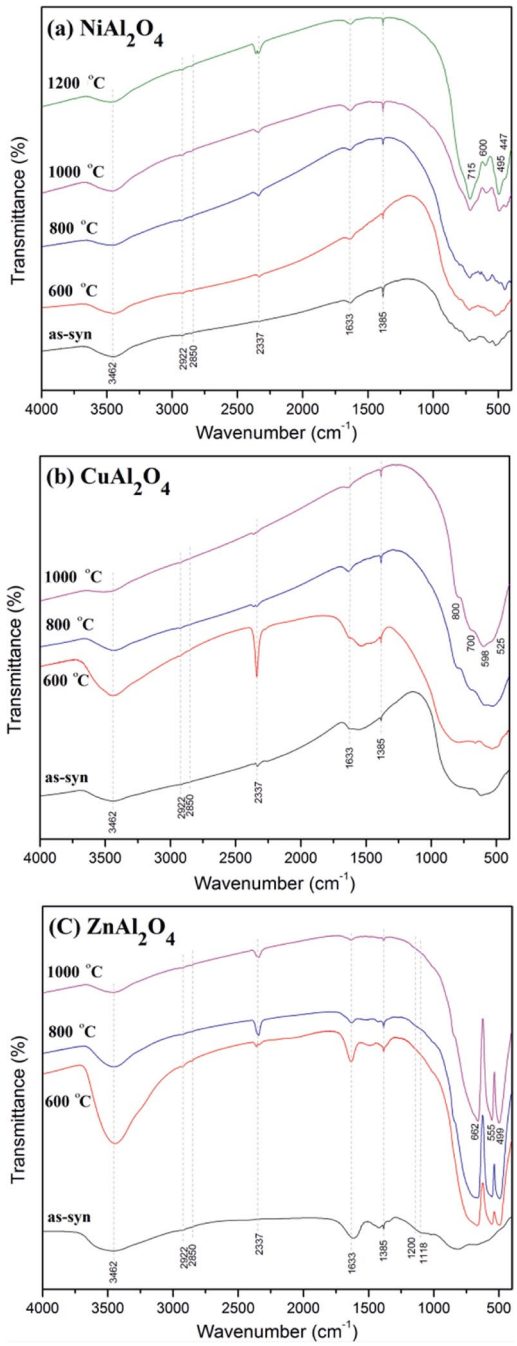

Fig. 2 FT-IR spectra of (a) $NiAl_2O_4$, (b) $CuAl_2O_4$, and (c) $ZnAl_2O_4$ powders calcined at different temperatures.

calcination time. This affected the improvement of absorption and transmittance efficiency resulting in an extensive number of electrical, optical, and catalytic applications. In the FT-IR spectrum of as-synthesized $NiAl_2O_4$ powders (Fig. 2(a)), several small absorption bands located in the range of 400–1000 cm^{-1} are assigned to the vibrational modes of NiO and Al_2O_3 [40,41]. These impurity bands remain in the samples calcined at 600 and 800 ℃. By increasing the calcination

temperature to 1000 and 1200 ℃, the characteristic bands of $NiAl_2O_4$ appear at around 715, 600, 495, and 447 cm^{-1}, which would confirm the formation of $NiAl_2O_4$ aluminate spinel structure, in good agreement with the XRD results [42,43]. These bands can be attributed to the symmetric stretching, bending, and asymmetric stretching modes of Ni–O, Al–O, and Ni–O–Al bonds at tetrahedral and octahedral sites in metal aluminate spinels [9,35,44]. Regarding the FT-IR spectrum of the as-synthesized $CuAl_2O_4$ powders (Fig. 2(b)), two broad bands corresponding to vibrational modes of CuO and Al_2O_3 are found at 1560 cm^{-1} and between 400 and 1000 cm^{-1} [41,45]. The intensity of CuO band at 1560 cm^{-1} slightly increases after calcination at 600 ℃ due to a higher degree of crystallinity. The FT-IR spectrum of $CuAl_2O_4$ calcined at 800 ℃ confirms the crystallization of spinel structure through the apparition of new bands at around 525, 598, 700, and 800 cm^{-1}, which are assigned to the Cu–O, Al–O, and Cu–O–Al vibrations [11,46]. These bands grow at the expense of the CuO band. As the calcination temperature increased to 1000 ℃, the CuO band disappears while the four characteristic bands of $CuAl_2O_4$ become stronger, indicating the complete transformation from CuO to $CuAl_2O_4$. These results correlate well with the XRD data, affirming the phase evolution and the formation of a single-phase $CuAl_2O_4$ spinel structure. For the $ZnAl_2O_4$ samples (Fig. 2(c)), the FT-IR spectrum of as-synthesized powders only shows broad bands between 1000 and 1200 cm^{-1} (C–O and C–C vibration) and at 816 cm^{-1} (NO_3^- vibration) including the three OH vibration bands mentioned above, which would indicate the amorphous character of the sample [35,36,47]. After calcination at 600 ℃, three well-defined characteristic bands describing the formation of the $ZnAl_2O_4$ spinel structure are observed in the range of 400–800 cm^{-1}. The bands located at 662, 555, and 499 cm^{-1} are attributed to the vibrations of Zn–O, Al–O, and Zn–O–Al bonds in ZnO_4 tetrahedra and AlO_6 octahedral groups in the spinel structure [9,35,44]. These bands become sharper as the calcination temperature increases to 800 and 1000 ℃, suggesting a high degree of crystallinity of zinc aluminate. No other impurity phases are found in the samples.

3. 3 SEM analysis

The morphologies of as-synthesized and calcined $NiAl_2O_4$, $CuAl_2O_4$, and $ZnAl_2O_4$ powders (no grinding) were examined using SEM, as shown in Fig. 3. SEM images of as-synthesized $NiAl_2O_4$ (Fig. 3(a)) and $CuAl_2O_4$ (Fig. 3(f)) show agglomerated particles with a rounded shape lying over a smooth surface. Two phases can be distinguished, which is consistent with XRD results revealing the coexistence of Al_2O_3 phase with their corresponding metal oxide phase, i.e., NiO and CuO for the as-synthesized $NiAl_2O_4$ and $CuAl_2O_4$, respectively. The particle size of spherical agglomerates is found to decrease with increasing temperature. Upon calcination at 800 ℃ (Figs. 3(c) and 3(h)), $NiAl_2O_4$ and $CuAl_2O_4$ samples are composed of several tiny spherical particles with grain sizes below 50 nm. A further increasing calcination temperature causes the formation of small spherical nanoparticles which are closely packed together with a homogeneous size distribution (Figs. 3(d), 3(e), and 3(i)). The average particle size of pure $NiAl_2O_4$ and $CuAl_2O_4$ nanopowders obtained at their respective optimum temperatures (1200 and 1000 ℃) are in the ranges of 20–50 nm and 100–200 nm. Regarding the development of $ZnAl_2O_4$ morphology, SEM image of as-synthesized amorphous powders (Fig. 3(j)) illustrates the presence of agglomerated particles with diverse sizes and shapes. As the calcination temperature increases to 1000 ℃ (Fig. 3(d)), the $ZnAl_2O_4$ particles become more uniform and spherical with mean particle size ca. 50 nm. In addition, the release of volatile gases such CO_2, N_2, O_2, and H_2O during the combustion process should be one of the main factors that create pores in the $NiAl_2O_4$, $CuAl_2O_4$ and $ZnAl_2O_4$ powders. This interconnected pore structure is important for catalytic applications.

3. 4 TEM analysis

In order to further confirm the nano-scale morphology of $NiAl_2O_4$, $CuAl_2O_4$, and $ZnAl_2O_4$ powders, TEM studies were carried out. Figure 4 illustrates TEM micrographs of the single-phase $NiAl_2O_4$ (Fig. 4(a)), $CuAl_2O_4$ (Fig. 4(b)), and $ZnAl_2O_4$ (Fig. 4(c)) powders calcined at 1200, 1000, and 1000℃, respectively. It was found that all samples were composed of polyhedral particles with particle size in the range of 40–60 nm.

3. 5 UV-DRS analysis

To understand the excitons and interband transitions, the UV-DRS spectra of $NiAl_2O_4$, $CuAl_2O_4$, and $ZnAl_2O_4$ powders calcined at different temperatures were measured in a wavelength range of 200–1000 nm, as shown in Fig. 5. Each metal aluminate displays different spectral profile with characteristic absorption bands. Figure 5(a) shows the UV-DRS spectra of as-synthesized and calcined

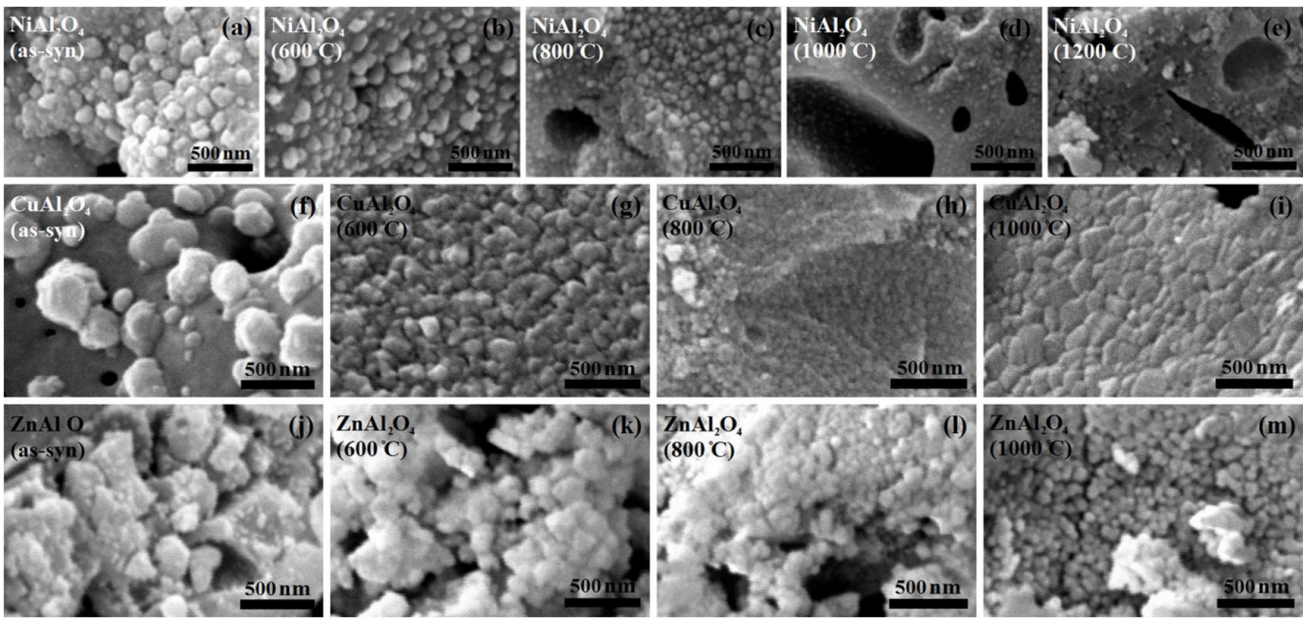

Fig. 3 SEM images of $NiAl_2O_4$, $CuAl_2O_4$, and $ZnAl_2O_4$ powders calcined at different temperatures.

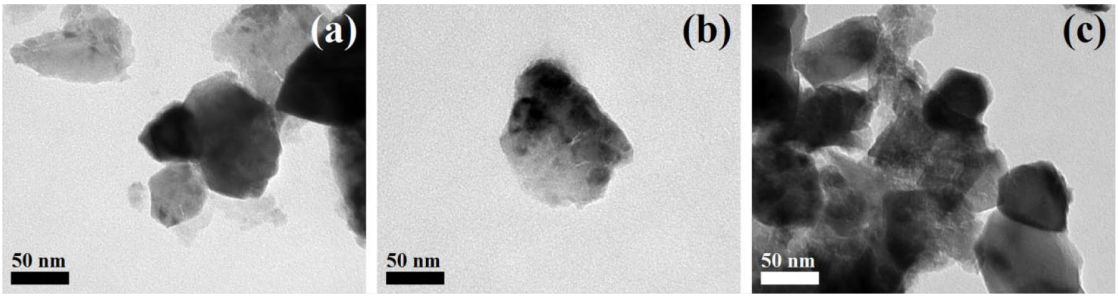

Fig. 4 TEM images of single-phase (a) $NiAl_2O_4$, (b) $CuAl_2O_4$, and (c) $ZnAl_2O_4$ powders.

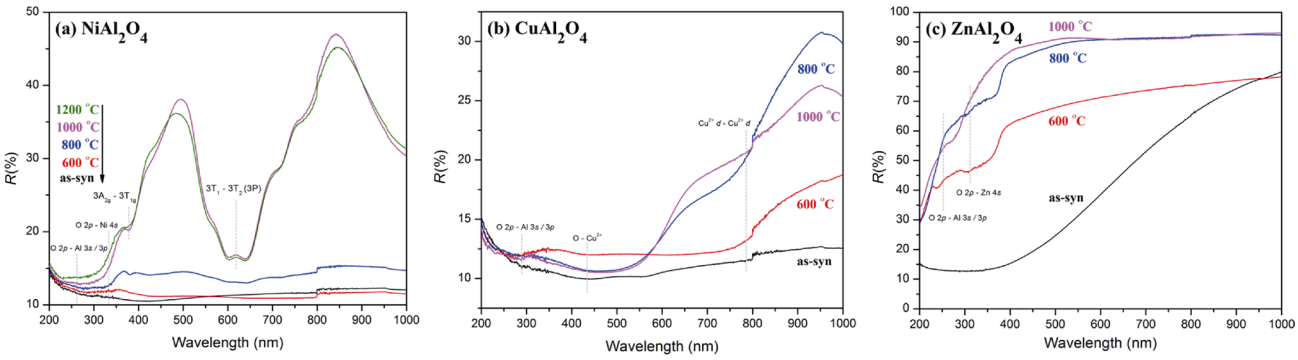

Fig. 5 UV-DRS diffuse reflectance spectra of (a) $NiAl_2O_4$, (b) $CuAl_2O_4$, and (c) $ZnAl_2O_4$ powders calcined at different temperatures.

$NiAl_2O_4$ powders. The powders calcined at 600 ℃ exhibit a broad absorption band with reflectance values of 10%–15% over the UV region up to the NIR region. After heating to 800 ℃, three small bands corresponding to the formation of $NiAl_2O_4$ spinel structure occur at about 380, 600, and 645 nm [22]. These characteristic bands become stronger when the calcination temperature increases to 1200 ℃. Many intense convoluted bands are located at about 240, 260, 380, 600, and 645 nm. The reflectance of both samples also increased sharply at wavelengths of 350–550 nm and 650–1000 nm up to maximum values of 37.5% and 47.5%, respectively.

This spectral evolution confirms the complete formation of a $NiAl_2O_4$ spinel structure [48]. The broad absorption bands located at 240 and 260 nm originate from the fundamental band-to-band electron transition between filled O 2p orbitals and empty Al 3s with the possibility of Al 3p wave function mixing. The additional shoulder observed at 320 nm is associated with electronic excitation between filled O 2p and empty Ni 4s orbitals [49]. This usually depends on the intrinsic defects of the sample. The high-energy band at 380 nm is associated with both the charge transfer bands and $3A_{2g}$–$3T_{1g}$ spin allowing transition for octahedral coordination of Ni^{2+} cations [48]. The bands at about 600 and 645 nm can be attributed to $3T_1$–$3T_2$ (3P) spin allowing transition. These doublet d–d bands can be related to Ni^{2+} in tetrahedral and octahedral sites, respectively [3,49], which would confirm an inverse spinel structure of $NiAl_2O_4$. For the $CuAl_2O_4$ samples (Fig. 5(b)), the UV-DRS spectrum of as-synthesised powders also exhibits a broad absorption band with about 10%–12.5% reflectance value covering spectra ranging from the UV up to the NIR region without any prominent features. An increase in calcination temperature to 600 ℃ results in the apparition of three small absorption bands at about 290, 440, and 750 nm [50]. These bands become stronger and more visible when $CuAl_2O_4$ samples are calcined at 800 ℃. Further heating to 1000 ℃, the characteristic band of CuO at 750 nm disappears, which would suggest the complete formation of the $CuAl_2O_4$ spinel structure. The high energy band at 290 nm is related to the fundamental electron transition between filled O 2p orbitals and empty Al 3s orbitals (which can be mixed with the 3*p* orbital), while the band at about 440 nm is associated with the charge transfer between O and Cu^{2+} occupied octahedral sites [51,52]. The new broad shoulder at around 800 nm corresponds to the Cu^{2+} d–d transitions in a tetragonally-distorted octahedral geometry around Cu^{2+} ions [27]. Moreover, it can be clearly seen that the reflectance percentage in the high wavelength VIS region (600–800 nm) and NIR region (800–1000 nm) of $CuAl_2O_4$ samples tends to increase with increasing calcination temperatures while that of the UV region (200–400 nm) and low wavelength VIS region (400–600 nm) is comparable (10%–12.5%) for all samples. Even though there are various hypotheses that have been proposed in order to explain the strong variation of the absorption band intensity, reasonable results were presented by le Nestour *et al.* [53]. Their $CuAl_2O_4$ samples prepared at 700 and 1000 ℃ exhibited different absorption behaviors in both VIS and NIR regions. Based on their electron paramagnetic resonance (EPR) spectra, they concluded that the Cu^{2+}/Cu^{+} mixed valencies and defects such as oxygen vacancies in the anion network of sample prepared at low temperature were responsible for this phenomena. The intra-atomic transition ($3d^{10}\rightarrow 4s^0$) in these monovalent copper cations (Cu^{+}) affect the increase in absorption intensity at around 780 nm. On the contrary, the calcination at 1000 ℃ leads to the oxidation reaction $Cu^{+}\rightarrow Cu^{2+} + e^{-}$. This increase of Cu^{2+} directly affects the inter-atomic d–d charge transfer between divalent and monovalent copper cations (Cu^{2+}/Cu^{+} intervalency transitions) that may be responsible for the variation of the absorption band from around 800 to 1000 nm. In the $ZnAl_2O_4$ samples (Fig. 5(c)), the reflectance of all samples increases with increasing calcination temperature in the overall wavelength region. The UV-DRS spectrum of amorphous powders shows a broad absorption band covering a range from the ultraviolet (UV) region up to the near-infrared (NIR) region without any significant features. After calcination at 600 ℃, $ZnAl_2O_4$ powders exhibit absorption bands at about 200, 250, 320, and 350 nm. The high-energy bands of $ZnAl_2O_4$ aluminate spinel are related to fundamental band-to-band electron excitation between filled O 2p orbitals and empty Al 3s orbitals, with the possibility of Al 3p wave function mixing [8,14]. The broad shoulder observed in the 320–350 nm wavelength region is typically associated with electronic transition between filled O 2p and empty Zn 4s orbitals depending on the intrinsic properties (spinel defects) [8,15]. This shoulder band is found to shift to a higher energy with increasing calcination temperatures. Both $ZnAl_2O_4$ samples calcined at 800 and 1000 ℃ show the maximum reflectance of 98% over the spectral range of 500–1000 nm. The significant increase in reflectance value in the VIS regions rendered these powders brighter and whiter when compared to ivory-colored samples calcined at 600 ℃, as illustrated in Fig. 6. Similar observation was reported by Cornu *et al.* [54], of which $ZnAl_2O_4$ powders were synthesized using Pechini method and calcined at different temperatures ranging from 600 to 1350 ℃ [54]. They found that reflectance percentages of $ZnAl_2O_4$ in the UV region (300–400 nm) and VIS region (400–550 nm) tended to increase with increasing calcination temperature and reached a maximum value of about 95%, while no modification was observed in the 200–300 nm region. They explained that these occurrences should be related to the disappearance of six fold-coordinated zinc ions. The Zn–O charge transfer band of six fold-coordinated zinc ions located at

Fig. 6 Photographs of $NiAl_2O_4$, $CuAl_2O_4$, and $ZnAl_2O_4$ powders calcined at different temperatures.

400–500 nm disappear while only the Zn–O charge transfer band of four fold-coordinated zinc ions remains visible below 300 nm, which confirms the complete formation of a $ZnAl_2O_4$ spinel structure.

3. 6 Optical band gap analysis

The optical band gaps of $NiAl_2O_4$, $CuAl_2O_4$, and $ZnAl_2O_4$ aluminate spinels are calculated from UV-DRS spectra. The Kubelka–Munk function is first applied to convert diffuse reflectance into an equivalent absorption coefficient for powder samples.

$$\alpha = F(R) = \frac{(1-R)^2}{2R} \tag{5}$$

where $F(R)$ is the Kubelka–Munk function, α is the absorption coefficient, and R is the reflectance. Therefore, the optical band gap can be determined by Tauc relation.

$$F(R)h\nu = A(h\nu - E_g)^n \tag{6}$$

where $h\nu$ is light energy, A is constant, E_g is band gap energy, n = 1/2 for direct band gap. Figure 7 displays the plots of $(F(R)h\nu)^2$ versus $h\nu$ for $NiAl_2O_4$, $CuAl_2O_4$, and $ZnAl_2O_4$ powders calcined at various temperatures. The extrapolation of Tauc plot to x axis provides the value of direct band gap energy (E_g). These results show that the band gap energies of all metal aluminate samples increase with increasing calcination temperature (Table 1). The $NiAl_2O_4$, $CuAl_2O_4$, and $ZnAl_2O_4$ calcined at the highest temperature exhibit a direct band gap of 3.45, 3.00, and 5.50 eV, respectively. The E_g value of our $NiAl_2O_4$ aluminate spinel (3.45 eV) agrees well with the previous study reported by Gouda and Bayoumy. [55] who applied combustion method using citric acid as fuel (3.4 eV). For the pure $ZnAl_2O_4$ powders calcined at 600–1000 ℃, they exhibit E_g values in the range of 5.35–5.50 eV which are slightly higher than those obtained by using urea as fuel (5.1 eV) [49]. However, the band gap energy of our $CuAl_2O_4$ powders is found to be larger than those prepared by conventional and microwave combustion methods using aloe vera extract as fuel (2.34–2.50 eV) [51,52]. This blue shift in the optical band gap may be attributed to the difference in particle size and size distribution which can cause inhomogeneous broadening of the optical spectra. Furthermore, the change in the band gap values would explain the color variation of metal aluminates with calcination temperature, as shown in Fig. 6. The band gap value of the as-synthesized $NiAl_2O_4$ sample is 1.65 eV, while increasing the calcination temperature to 1200 ℃ the band gap expands to 3.45 eV. These

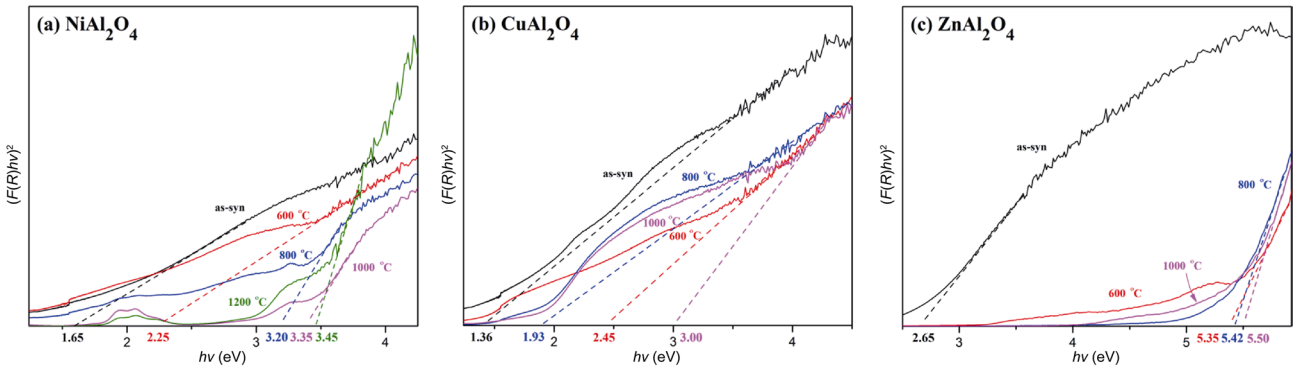

Fig. 7 Plot of $(F(R)hv)^2$ vs. hv for (a) $NiAl_2O_4$, (b) $CuAl_2O_4$, and (c) $ZnAl_2O_4$ powders calcined at different temperatures.

results are directly related to a blue shift of the absorption wavelength which enhances the cerulean blue color of the pure $NiAl_2O_4$ samples. A blue shift in absorbance wavelength also causes the change of color in $CuAl_2O_4$ samples from the black as-synthesized powders to black olive and red-brown $CuAl_2O_4$ powders. Thus, the color variation can be a direct evidence for the impact of calcination temperature on the respective aluminates.

3. 7 PL analysis

PL spectra were recorded to investigate the recombination phenomena in the samples. From these spectra, it is possible to obtain the information of band gap with the relative energy position of sub-band gap defect states [56] in materials which can be influenced by the synthesis condition [49]. Figure 8 shows the room temperature normalized PL spectra of single-phase $NiAl_2O_4$ (Fig. 8(a)), $CuAl_2O_4$ (Fig. 8(b)), and $ZnAl_2O_4$ (Fig. 8(c)), recorded with 225 nm excitation wavelength. All samples show violet, blue, and green emission bands from 360 to 560 nm. $NiAl_2O_4$ exhibits weak broad luminescence bands with a sharp blue emission peak at 475 nm. Whereas, $ZnAl_2O_4$ and $CuAl_2O_4$ powders show high intensity of violet emission centered at about 425 and 440 nm, respectively. The intensity of the PL peak is known to be controlled by the number of charge transfers and surface defects, including the existence of some organic residual (e.g., NO_3^- and CO_2) previously observed in the FT-IR results [57,58]. The emission peaks that occurred in the PL spectra of each metal aluminate samples are attributed to the recombination of electrons and photogenerated holes involving various structural defects, such as the ionized charge states of intrinsic defects, oxygen vacancies, metal (Ni, Cu, Zn) vacancy, metal interstitials, and oxygen antisites. Rapid combustion during the sol-gel auto combustion method usually generates these structural defects, which act as deep defect donors in semiconductor oxides and contribute to the optical emission [59]. The intensities (I) of the strongest emission peak of the as-synthesized and calcined aluminate samples, including their fluorescence lifetime (τ), are tabulated in Table 2. The fluorescence intensity values of single-phase aluminate samples are in accordance with Wang *et al.* [58], Kool *et al.* [60], and He *et al.* [61] whose $NiAl_2O_4$, $CuAl_2O_4$, and $ZnAl_2O_4$ samples were prepared by the modified sol-gel and co-precipitation methods. Moreover, the fluorescence lifetime tends to increase with increasing

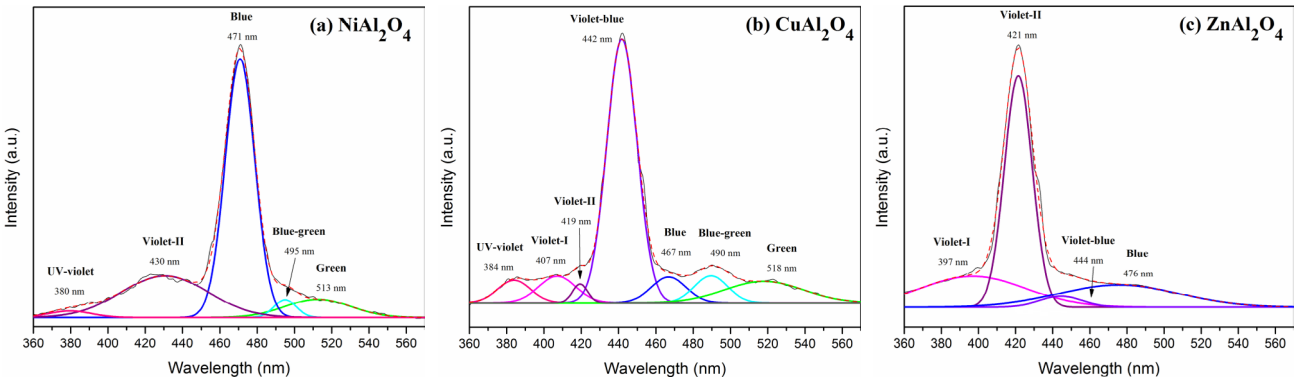

Fig. 8 Deconvoluted PL emission spectra of single-phase (a) $NiAl_2O_4$, (b) $CuAl_2O_4$, and (c) $ZnAl_2O_4$ powders.

Table 2 Photoluminescence intensity (*I*) and fluorescence lifetime (*τ*) of (a) $NiAl_2O_4$, (b) $CuAl_2O_4$, and (c) $ZnAl_2O_4$ powders calcined at different temperatures

Sample	As-syn.		600 ℃		800 ℃		1000 ℃		1200 ℃	
	I (a.u.)	*τ* (ms)	*I* (a.u.)	*τ* (ms)	*I* (a.u.)	*τ* (ms)	*I* (a.u.)	*τ* (ms)	*I* (a.u.)	*τ* (ms)
$NiAl_2O_4$	264	0.3752	287	0.4757	326	0.6838	411	0.8853	448	0.9055
$CuAl_2O_4$	318	0.1803	320	0.2384	344	0.5389	364	0.9172	—	—
$ZnAl_2O_4$	316	0.0642	1302	0.2139	1490	0.2255	1646	0.2764	—	—

calcination temperature. Yin *et al.* [62] reported that these occurrences may be related to the increase of crystal field effects on the energy level within the matrix leading to the transition change and having an impact on the lifetime of the excited state electrons.

All the PL spectra between 360 and 560 nm can be deconvoluted into several emission peaks centered at 382 nm (3.25 eV), 402 nm (3.08 eV), 423 nm (2.03 eV), 443 nm (2.8 eV), 471 nm (2.63 eV), 493 nm (2.52), and 516 nm (2.4 eV) which are denoted by UV-violet, violet-I, violet-II, violet-blue, blue, blue-green, and green emissions, respectively. Deconvolution of the PL spectrum for $NiAl_2O_4$ is depicted in Fig. 8(a). A good fit is achieved with five Gaussian components centered at 380 nm (UV-violet), 430 nm (violet-II), 471 nm (blue), 495 nm (blue-green), and 513 nm (green). The single-phase $CuAl_2O_4$ spectrum (Fig. 8(b)) gives seven emission peaks at 384 nm (UV-violet), 407 nm (violet-I), 419 nm (violet-II), 442 nm (violet-blue), 467 nm (blue), 490 nm (blue-green), and 518 nm (green). For $ZnAl_2O_4$ aluminate calcined at 600 ℃ (Fig. 8(c)), the PL spectrum is deconvoluted into four emission peaks centered at 397 nm (violet-I), 421 nm (violet-II), 444 nm (violet-blue), and 476 nm (blue).

To better understand the fluorescence mechanism of the $NiAl_2O_4$, $CuAl_2O_4$, and $ZnAl_2O_4$ samples, a schematic band diagram as shown in Fig. 9 is created to show the excitation and emission processes. When the E_g value of metal aluminates (3.45 eV for $NiAl_2O_4$, 3.00 eV for $CuAl_2O_4$, and 5.35 eV for $ZnAl_2O_4$) is lower than the excitation wavelength (λ_{ex} = 225 nm, 5.51 eV), an electron in the valence band (VB) can be excited to higher energy levels in the conduction band (CB) and then falls to the conduction band maximum (CBM) through internal conversion (IC) (Fig. 9(a)) and vibrational relaxation (VR). The electron at CBM can then radiatively recombine with a hole in the valence band or defect states in the band gap resulting in the UV-violet, violet-I, violet-II, violet-blue, blue, blue-green, and green light emissions.

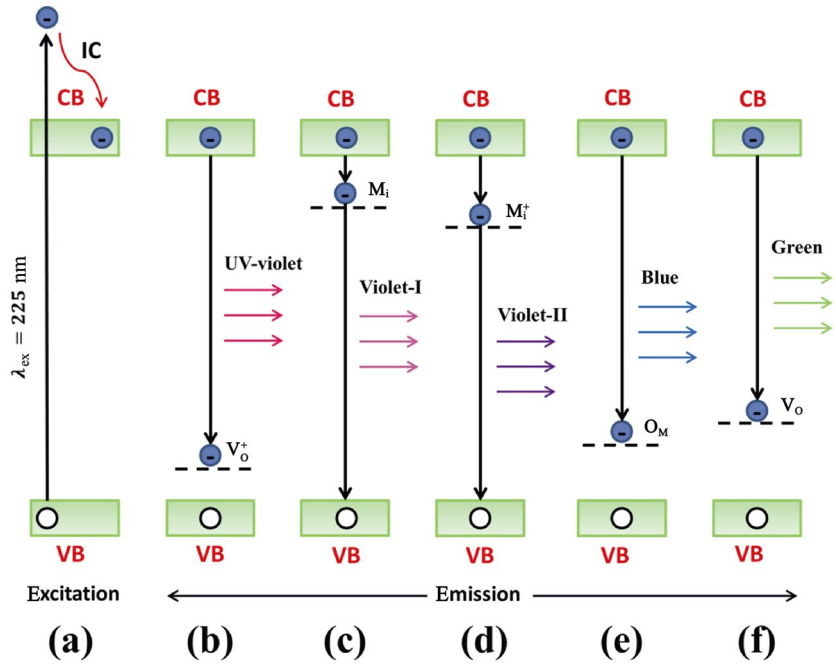

Fig. 9 Fluorescence mechanism, presenting various PL emission components originated due to electronic transitions between different defect levels and the band edges of aluminate powders.

The origin of the individual components of luminescence emission has been analyzed from the available energy positions of various defect centers existing within the Zn–O, Ni–O, and Cu–O systems [53,63–66]. The UV-violet emission luminescence peak at about 380 nm (~3.26 eV) can be attributed to electron transition from the CB to a single ionized oxygen vacancy (V_O^+) as the responsible acceptor defects located at 0.27 eV above the VB (Fig. 9(b)) [67]. Two satellite components of violet luminescence are visible in each spectrum. The violet-I luminescence peak at 397 to 407 nm (3.05 to 3.12 eV) occurs through possible transition of electrons trapped at metal interstitial (M_i) defects to the VB (Fig. 9(c)), while the violet-II luminescence peak at 419 to 430 nm (2.88 to 2.96 eV) arises through possible electron transition between the ionized metal interstitial (M_i^+) defects level and the VB (Fig. 9(d)). This assumptions is in agreement with the previous study reported by Zeng *et al.* [68] that the violet-blue emission can be interpreted by the transition of extended metal interstitials (M_i) states lying below the conduction band minima. Kim *et al.* [69] have also calculated the formation enthalpy of a complex of V_O and doubly ionized M_i^{++} defect. They found that each complex will generate pairs of M_i^* and V_O^* states differing slightly in energy from other complex. The electron–hole recombination between these M_i^* states and the VB led to the origin of violet-blue emission. Regarding the origin of the blue emission, several hypotheses have been proposed including electron transition from oxygen vacancies (V_O) to the VB, metal interstitials (M_i) to metal vacancies (V_M), and M_i to the VB or –OH groups at the particle surface which vary according to the synthesis techniques [70–73]. The blue emission was observed for ZnO particles synthesized by sol-gel method in the presence of Li^+ cations and excessive OH^- anions that caused a stoichiometric excess of oxygen favoring the formation of specific defects, including interstitial oxygen (O_i), oxygen antisite (O_{Zn}), and different zinc vacancies (V_{Zn}^O; V_{Zn}^-; V_{Zn}^{2-}) [74]. Since most of these defects are acceptors in nature, the possible path for the blue emission is the conduction-band-to-acceptor transitions. Moreover, the density functional theory (DFT) calculation confirmed that energy levels of O_i, O_{Zn}, V_{Zn}^O, V_{Zn}^-, and V_{Zn}^{2-} are 3.06, 2.66, 0.56, 2.28 and 2.38 eV below the CB, respectively. The previous research on the defect-related photoluminescence behavior of Ni–O and Cu–O systems by Anbuselvan *et al.* [75,76] also gave concordant results for the blue emission. Therefore, the blue luminescence peak of our metal aluminates appearing at 2.61 to 2.66 eV (467–476 nm) can be attributed to oxygen antisites (O_M) as the responsible acceptor defects (Fig. 9(e)). Van Dijken *et al.* [77], Mochizuki and Saito. [78], and Zhao *et al.* [76] explained the phenomenon of the origin of green emission at around 500 nm by the recombination of a shallowly trapped electron with a deeply trapped hole. The photogenerated hole is first trapped at the surface of the nanoparticles by surface defects such as O^{2-}/O^- and then migrates to vacancy levels located deep in the particle leading to the formation of a deep hole trapped level above the VB (Fig. 9(f)). Emission at around 500 nm (~2.48 eV) occurs when the photogenerated hole trapped in the deep oxygen vacancy recombines with the photogenerated electron trapped in a shallow level located just below the CB.

4 Conclusions

$NiAl_2O_4$, $CuAl_2O_4$, and $ZnAl_2O_4$ aluminate spinel nanoparticles were successfully synthesized by the sol-gel auto combustion method using DEA as a fuel. The calcination temperature is found to strongly influence the phase formation, particle size, optical, and fluorescence properties of the final product. The XRD results affirm that the formation of single-phase $NiAl_2O_4$, $CuAl_2O_4$, and $ZnAl_2O_4$ spinel structures occurs at 1200, 1000, and 600 ℃, respectively. The characteristic IR absorption bands in the frequency range of 400–800 cm^{-1} confirm the formation of a spinel structure, while SEM and TEM images depict the formation of well-developed nanosized grains. Their porous structures would enable these aluminate spinels to serve as a potential candidate in the adsorption and catalytic applications. The UV–visible diffuse reflectance spectra illustrate dramatic improvement of reflectance in the visible and infrared regions up to 90% for the $ZnAl_2O_4$ sample calcined at 1000 ℃ and around 40% for the single-phase $NiAl_2O_4$ sample; meanwhile, all $CuAl_2O_4$ samples show strong absorption in both UV and visible regions with maximum value of 90%, while improvement of reflectance in the infrared region of up to 30% is obtained with increasing calcination temperature. The optical band gap values of all samples are found to increase with increasing calcination temperature. The photoluminescence analysis of metal aluminate spinels reveals that the $ZnAl_2O_4$ powders exhibit interesting abilities for applications in

violet and blue light-emitting devices, while $NiAl_2O_4$ and $CuAl_2O_4$ powders are capable to provide violet, blue, and green emissions for potential use as fluorescent materials. Moreover, the sol-gel auto combustion method can be considered a very effective and useful technique to synthesize other metal aluminate nanoparticles with good optoelectronic properties.

Acknowledgements

This work has been financially supported by Faculty of Science at Sriracha, Kasetsart University, Sriracha Campus and the Kasetsart University Research and Development Institute (KURDI), Bangkok, Thailand.

References

[1] Sharma RK, Ghose R. Synthesis and characterization of nanocrystalline zinc aluminate spinel powder by sol–gel method. *Ceram Int* 2014, **40**: 3209–3214.

[2] Ravikumar BS, Nagabhushana H, Sharma SC, *et al*. *Calotropis procera* mediated combustion synthesis of $ZnAl_2O_4$: Cr^{3+} nanophosphors: Structural and luminescence studies. *Spectrochimica Acta Part Mol Biomol Spectrosc* 2015, **136**: 1027–1037.

[3] Bayal N, Jeevanandam P. Synthesis of metal aluminate nanoparticles by sol–gel method and studies on their reactivity. *J Alloys Compd* 2012, **516**: 27–32.

[4] Han M, Wang ZS, Xu Y, *et al*. Physical properties of $MgAl_2O_4$, $CoAl_2O_4$, $NiAl_2O_4$, $CuAl_2O_4$, and $ZnAl_2O_4$ spinels synthesized by a solution combustion method. *Mater Chem Phys* 2018, **215**: 251–258.

[5] Ianoş R, Băbuţă R, Păcurariu C, *et al*. Combustion synthesis of $ZnAl_2O_4$ powders with tuned surface area. *Ceram Int* 2017, **43**: 8975–8981.

[6] Su SY, Wang SS, Sakthinathan S, *et al*. Preparation of $CuAl_2O_4$ submicron tubes from electrospun Al_2O_3 fibers. *Ceram Int* 2019, **45**: 1439–1442.

[7] Javanmardi M, Emadi R, Ashrafi H. Synthesis of nickel aluminate nanoceramic compound from aluminum and nickel carbonate by mechanical alloying with subsequent annealing. *Trans Nonferrous Met Soc China* 2016, **26**: 2910−2915.

[8] Stringhini FM, Foletto EL, Sallet D, *et al*. Synthesis of porous zinc aluminate spinel ($ZnAl_2O_4$) by metal-chitosan complexation method. *J Alloys Compd* 2014, **588**: 305–309.

[9] Davar F, Salavati-Niasari M. Synthesis and characterization of spinel-type zinc aluminate nanoparticles by a modified sol–gel method using new precursor. *J Alloys Compd* 2011, **509**: 2487–2492.

[10] Quirino MR, Oliveira MJC, Keyson D, *et al*. Synthesis of zinc aluminate with high surface area by microwave hydrothermal method applied in the transesterification of soybean oil (biodiesel). *Mater Res Bull* 2016, **74**: 124–128.

[11] Lv W, Luo ZK, Yang H, *et al*. Effect of processing conditions on sonochemical synthesis of nanosized copper aluminate powders. *Ultrason Sonochemistry* 2010, **17**: 344–351.

[12] Ianoş R, Borcănescu S, Lazău R. Large surface area $ZnAl_2O_4$ powders prepared by a modified combustion technique. *Chem Eng J* 2014, **240**: 260–263.

[13] Ragupathi C, Vijaya JJ, Kennedy LJ. Synthesis, characterization of nickel aluminate nanoparticles by microwave combustion method and their catalytic properties. *Mater Sci Eng B* 2014, **184**: 18–25.

[14] Visinescu D, Jurca B, Ianculescu A, *et al*. Starch-A suitable fuel in new low-temperature combustion-based synthesis of zinc aluminate oxides. *Polyhedron* 2011, **30**: 2824–2831.

[15] Anand GT, Kennedy LJ, Vijaya JJ, *et al*. Structural, optical and magnetic characterization of $Zn_{1-x}Ni_xAl_2O_4$ ($0\leq x\leq 5$) spinel nanostructures synthesized by microwave combustion technique. *Ceram Int* 2015, **41**: 603–615.

[16] Mimani T. Instant synthesis of nanoscale spinel aluminates. *J Alloys Compd* 2001, **315**: 123–128.

[17] Tangcharoen T, T-Thienprasert J, Kongmark C. Optical properties and versatile photocatalytic degradation ability of MAl_2O_4 (M = Ni, Cu, Zn) aluminate spinel nanoparticles. *J Mater Sci: Mater Electron* 2018, **29**: 8995–9006.

[18] Aguilar CG, Moreno CE, Castillo MP, *et al*. Effect of calcination temperature on structure and thermoelectric properties of $CuAlO_2$ powders. *J Mater Sci* 2018, **53**: 1646–1657.

[19] Nazemi MK, Sheibani S, Rashchi F, *et al*. Preparation of nanostructured nickel aluminate spinel powder from spent NiO/Al_2O_3 catalyst by mechano-chemical synthesis. *Adv Powder Technol* 2012, **23**: 833–838.

[20] Cornu L, Gaudon M, Jubera V. $ZnAl_2O_4$ as a potential sensor: Variation of luminescence with thermal history. *J Mater Chem C* 2013, **1**: 5419–5428.

[21] He Y, Shih K. Nano-indentation on nickel aluminate spinel and the influence of acid and alkaline attacks on the spinel surface. *Ceram Int* 2012, **38**: 3121–3128.

[22] Ragupathi C, Vijaya JJ, Surendhar P, *et al*. Comparative investigation of nickel aluminate ($NiAl_2O_4$) nano and microstructures for the structural, optical and catalytic properties. *Polyhedron* 2014, **72**: 1–7.

[23] Kumar RT, Suresh P, Selvam NCS, *et al*. Comparative study of nano copper aluminate spinel prepared by sol–gel and modified sol–gel techniques: Structural, electrical, optical and catalytic studies. *J Alloys Compd* 2012, **522**: 39–45.

[24] Koonsaeng N, Laobuthee A, Hasin P. Controllable synthesis of metallo-alkoxide precursor-derived nickel aluminate spinels using TEA-gel process and morphology-dependent reducibility. *Mater Chem Phys* 2016, **182**: 287–297.

[25] Hu CY, Shih K, Leckie JO. Formation of copper aluminate

spinel and cuprous aluminate delafossite to thermally stabilize simulated copper-laden sludge. *J Hazard Mater* 2010, **181**: 399–404.

[26] Arjmand M, Azad AM, Leion H, *et al*. Evaluation of $CuAl_2O_4$ as an oxygen carrier in chemical-looping combustion. *Ind Eng Chem Res* 2012, **51**: 13924–13934.

[27] Mindru I, Gingasu D, Patron L, *et al*. Copper aluminate spinel by soft chemical routes. *Ceram Int* 2016, **42**: 154–164.

[28] Kumar JP, Prasad GK, Allen JA, *et al*. Synthesis of mesoporous metal aluminate nanoparticles and studies on the decontamination of sulfur mustard. *J Alloys Compd* 2016, **662**: 44–53.

[29] Van der Laag NJ, Snel MD, Magusin PCMM, *et al*. Structural, elastic, thermophysical and dielectric properties of zinc aluminate ($ZnAl_2O_4$). *J Eur Ceram Soc* 2004, **24**: 2417–2424.

[30] Farhadi S, Panahandehjoo S. Spinel-type zinc aluminate ($ZnAl_2O_4$) nanoparticles prepared by the co-precipitation method: A novel, green and recyclable heterogeneous catalyst for the acetylation of amines, alcohols and phenols under solvent-free conditions. *Appl Catal A: Gen* 2010, **382**: 293–302.

[31] Fabián M, Bottke P, Girman V, *et al*. A simple and straightforward mechanochemical synthesis of the far-from-equilibrium zinc aluminate, $ZnAl_2O_4$, and its response to thermal treatment. *RSC Adv* 2015, **5**: 54321–54328.

[32] Parra MR, Haque FZ. Aqueous chemical route synthesis and the effect of calcination temperature on the structural and optical properties of ZnO nanoparticles. *J Mater Res Technol* 2014, **3**: 363–369.

[33] Stella KC, Nesaraj AS. Effect of fuels on the combustion synthesis of $NiAl_2O_4$ spinel particles. *Iran J Mater Sci Eng* 2010, **7**: 36–44.

[34] Gilabert J, Palacios MD, Sanz V, *et al*. Fuel effect on solution combustion synthesis of $Co(Cr,Al)_2O_4$ pigments. *Boletín De La Sociedad Española De Cerámica Y Vidrio* 2017, **56**: 215–225.

[35] Ge DL, Fan YJ, Qi CL, *et al*. Facile synthesis of highly thermostable mesoporous $ZnAl_2O_4$ with adjustable pore size. *J Mater Chem A* 2013, **1**: 1651–1658.

[36] Wei XH, Chen DH. Synthesis and characterization of nanosized zinc aluminate spinel by sol–gel technique. *Mater Lett* 2006, **60**: 823–827.

[37] Dolla TH, Pruessner K, Billing DG, *et al*. Sol-gel synthesis of $Mn_xNi_{1-x}Co_2O_4$ spinel phase materials: Structural, electronic, and magnetic properties. *J Alloys Compd* 2018, **742**: 78–89.

[38] Pedram MZ, Omidkhah M, Amooghin AE. Synthesis and characterization of diethanolamine-impregnated cross-linked polyvinylalcohol/glutaraldehyde membranes for CO_2/CH_4 separation. *J Ind Eng Chem* 2014, **20**: 74–82.

[39] Shanaj BR, John XR. Effect of calcination time on structural, optical and antimicrobial properties of nickel oxide nanoparticles. *J Theor Comput Sci* 2016, **3**: 1000149.

[40] Alagiri M, Ponnusamy S, Muthamizhchelvan C. Synthesis and characterization of NiO nanoparticles by sol–gel method. *J Mater Sci: Mater Electron* 2012, **23**: 728–732.

[41] Boumaza A, Djelloul A, Guerrab F. Specific signatures of α-alumina powders prepared by calcination of boehmite or gibbsite. *Powder Technol* 2010, **201**: 177–180.

[42] Samkaria R, Sharma V. Effect of rare earth yttrium substitution on the structural, dielectric and electrical properties of nanosized nickel aluminate. *Mater Sci Eng B* 2013, **178**: 1410–1415.

[43] Buvaneswari G, Aswathy V, Rajakumari R. Comparison of color and optical absorbance properties of divalent ion substituted Cu and Zn aluminate spinel oxides synthesized by combustion method towards pigment application. *Dye Pigment* 2015, **123**: 413–419.

[44] Staszak W, Zawadzki M, Okal J. Solvothermal synthesis and characterization of nanosized zinc aluminate spinel used in iso-butane combustion. *J Alloys Compd* 2010, **492**: 500–507.

[45] Kayani ZN, Umer M, Riaz S, *et al*. Characterization of copper oxide nanoparticles fabricated by the sol-gel method. *Journal of Electronic Materials* 2015, **44**: 3704–3709.

[46] Salavati-Niasari M, Davar F, Farhadi M. Synthesis and characterization of spinel-type $CuAl_2O_4$ nanocrystalline by modified sol–gel method. *J Sol-Gel Sci Technol* 2009, **51**: 48–52.

[47] Wahab R, Kim YS, Shin HS. Synthesis, characterization and effect of pH variation on zinc oxide nanostructures. *Mater Trans* 2009, **50**: 2092–2097.

[48] Ragupathi C, Vijaya JJ, Kennedy LJ. Preparation, characterization and catalytic properties of nickel aluminate nanoparticles: A comparison between conventional and microwave method. *J Saudi Chem Soc* 2017, **21**: S231–S239.

[49] Anand GT, Kennedy LJ, Aruldoss U, *et al*. Structural, optical and magnetic properties of $Zn_{1-x}Mn_xAl_2O_4$ ($0 \leqslant x \leqslant 0.5$) spinel nanostructures by one-pot microwave combustion technique. *J Mol Struct* 2015, **1084**: 244–253.

[50] Białas A, Kuśtrowski P, Dudek B, *et al*. Copper-aluminum oxide catalysts for total oxidation of toluene synthesized by thermal decomposition of co-precipitated precursors. *Thermochimica Acta* 2014, **590**: 191–197.

[51] Ragupathi C, Vijaya JJ, Kennedy LJ, *et al*. Nanostructured copper aluminate spinels: Synthesis, structural, optical, magnetic, and catalytic properties. *Mater Sci Semicond Process* 2014, **24**: 146–156.

[52] Ragupathi C, Judith Vijaya J, Thinesh Kumar R, *et al*. Selective liquid phase oxidation of benzyl alcohol catalyzed by copper aluminate nanostructures. *J Mol Struct* 2015, **1079**: 182–188.

[53] Le Nestour A, Gaudon M, Villeneuve G, *et al*. Defects in divided zinc–copper aluminate spinels: Structural features and optical absorption properties. *Inorg Chem* 2007, **46**: 4067–4078.

[54] Cornu L, Duttine M, Gaudon M, *et al*. Luminescence switch of Mn-doped $ZnAl_2O_4$ powder with temperature. *J Mater Chem C* 2014, **2**: 9512–9522.

[55] Gouda ME, Bayoumy WAA. Structural, optical and magnetic properties of Ni aluminates with Co substitution. *Int J Sci Eng Res* 2015, **6**: 328–332.

[56] Anand GT, Kennedy LJ, Vijaya JJ. Microwave combustion synthesis, structural, optical and magnetic properties of $Zn_{1-x}Co_xAl_2O_4$ ($0 \leqslant x \leqslant 0.5$) spinel nanostructures. *J Alloys Compd* 2013, **581**: 558–566.

[57] Ragupathi C, Vijaya JJ, Narayanan S, *et al*. Catalytic properties of nanosized zinc aluminates prepared by green process using *Opuntia dilenii* haw plant extract. *Chin J Catal* 2013, **34**: 1951–1958.

[58] Wang SF, Sun GZ, Fang LM, *et al*. A comparative study of $ZnAl_2O_4$ nanoparticles synthesized from different aluminum salts for use as fluorescence materials. *Sci Rep* 2015, **5**: 12849.

[59] Ragupathi C, John Kennedy L, Judith Vijaya J. A new approach: Synthesis, characterization and optical studies of nano-zinc aluminate. *Adv Powder Technol* 2014, **25**: 267–273.

[60] Kool A, Thakur P, Bagchi B, *et al*. Sol–gel synthesis of transition-metal ion conjugated alumina-rich mullite nanocomposites with potential mechanical, dielectric and photoluminescence properties. *RSC Adv* 2015, **5**: 104299–104313.

[61] He C, Ji HP, Huang ZH, *et al*. Preparation and photoluminescence properties of red-emitting phosphor $ZnAl_2O_4$: Eu^{3+} with an intense $^5D_0 \rightarrow {}^7F_2$ transition. *Mater Res Express* 2018, **5**: 025501.

[62] Yin HR, Li YX, Bai JG, *et al*. Effect of calcinations temperature on the luminescence intensity and fluorescent lifetime of Tb^{3+}-doped hydroxyapatite (Tb-HA) nanocrystallines. *J Materiomics* 2017, **3**: 144–149.

[63] Willander M, Nur O, Sadaf JR, *et al*. Luminescence from zinc oxide nanostructures and polymers and their hybrid devices. *Materials* 2010, **3**: 2643–2667.

[64] Xu PS, Sun YM, Shi CS, *et al*. The electronic structure and spectral properties of ZnO and its defects. *Nucl Instruments Methods Phys Res Sect B Beam Interactions Mater Atoms* 2003, **199**: 286–290.

[65] Kumari L, Li WZ, Vannoy CH, *et al*. Vertically aligned and interconnected nickel oxide nanowalls fabricated by hydrothermal route. *Cryst Res Technol* 2009, **44**: 495–499.

[66] Madhu G, Biju V. Effect of Ni^{2+} and O^{2-} vacancies on the electrical and optical properties of nanostructured nickel oxide synthesized through a facile chemical route. *Phys E Low-dimensional Syst Nanostructures* 2014, **60**: 200–205.

[67] Das D, Mondal P. Low temperature grown ZnO: Ga films with predominant *c*-axis orientation in wurtzite structure demonstrating high conductance, transmittance and photoluminescence. *RSC Adv* 2016, **6**: 6144–6153.

[68] Zeng HB, Duan GT, Li Y, *et al*. Blue luminescence of ZnO nanoparticles based on non-equilibrium processes: Defect origins and emission controls. *Adv Funct Mater* 2010, **20**: 561–572.

[69] Kim YS, Park CH. Rich variety of defects in ZnO via an attractive interaction between O vacancies and Zn interstitials: Origin of *n*-type doping. *Phys Rev Lett* 2009, **102**: 086403.

[70] Zhang LY, Yin LW, Wang CX, *et al*. Origin of visible photoluminescence of ZnO quantum dots: Defect-dependent and size-dependent. *J Phys Chem C* 2010, **114**: 9651–9658.

[71] Ahn CH, Kim YY, Kim DC, *et al*. A comparative analysis of deep level emission in ZnO layers deposited by various methods. *J Appl Phys* 2009, **105**: 013502.

[72] Abdullah M, Lenggoro IW, Okuyama K, *et al*. In situ synthesis of polymer nanocomposite electrolytes emitting a high luminescence with a tunable wavelength. *J Phys Chem B* 2003, **107**: 1957–1961.

[73] Monticone S, Tufeu R, Kanaev AV. Complex nature of the UV and visible fluorescence of colloidal ZnO nanoparticles. *J Phys Chem B* 1998, **102**: 2854–2862.

[74] Han LL, Cui L, Wang WH, *et al*. On the origin of blue emission from ZnO quantum dots synthesized by a sol–gel route. *Semicond Sci Technol* 2012, **27**: 065020.

[75] Anbuselvan D, Muthukumaran S. Defect related microstructure, optical and photoluminescence behaviour of Ni, Cu co-doped ZnO nanoparticles by co-precipitation method. *Opt Mater* 2015, **42**: 124–131.

[76] Zhao XH, Wang P, Yan ZX, *et al*. Room temperature photoluminescence properties of CuO nanowire arrays. *Opt Mater* 2015, **42**: 544–547.

[77] Van Dijken A, Meulenkamp EA, Vanmaekelbergh D, *et al*. The kinetics of the radiative and nonradiative processes in nanocrystalline ZnO particles upon photoexcitation. *J Phys Chem B* 2000, **104**: 1715–1723.

[78] Mochizuki S, Saito T. Intrinsic and defect-related luminescence of NiO. *Phys B Condens Matter* 2009, **404**: 4850–4853.

Open Access This article is licensed under a Creative Commons Attribution 4.0 International License, which permits use, sharing, adaptation, distribution and reproduction in any medium or format, as long as you give appropriate credit to the original author (s) and the source, provide a link to the Creative Commons licence, and indicate if changes were made.

The images or other third party material in this article are included in the article's Creative Commons licence, unless indicated otherwise in a credit line to the material. If material is not included in the article's Creative Commons licence and your intended use is not permitted by statutory regulation or exceeds the permitted use, you will need to obtain permission directly from the copyright holder.

To view a copy of this licence, visit http://creativecommons.org/licenses/by/4.0/.